 doi:10.20944/preprints202205.0401.v1

Article

Optimization and Hydration Mechanism of Ecological Ternary Cements Containing Phosphogypsum

Jiaojiao Hou [1,2]*, Xiaoyang Ni [1], Baosong Ma [2]

[1] Faculty of Engineering, China University of Geosciences, Wuhan 430074, China
[2] School of Civil Engineering, Sun Yat-Sen University, Guangzhou 510275, China
* Correspondence: houxw3000@cug.edu.cn

Abstract: Ecological ternary cements (ECP) were perpared with powders of phosphogypsum (PG), fly ash (FA) and portland cement (PC). The evolution mechanism of the hydration product structure was characterized through macro and micro experiments.The thermodynamic characteristics of solid phase, solid solution phase and aqueous solution in process of hydration about phosphogypsum-fly ash-cement ternary cementitious system were studied based on the Gibbs-free-energy C-S-H thermodynamic model and GEM-Selektor software, and compared with experimental results. The results show that in the hydration reaction the thermodynamic interaction between mineral single-phase and hydration products plays an important role in the spatio-temporal distribution of ions in the cementitious system. The values of CaO, SiO2Hand H2Ohyd gradually increased with the increase of Ca/Si ratio, while the values of CaOext and H2OOH showed a positive proportional relationship, and the values of SiO2H and SiO2 showed an inverse proportional relationship. GEM-Selektor is accurate in the simulation calculation of the total amount of AFt and AFm mineral phases which quantitatively analysis the correlation between C-S-H gels formation and C3S with complex decomposition ion groups.

Keywords: ecological cement; cementitious system; thermodynamic; calcium silicate hydrate; tricalcium silicate; GEM-Selektor

1. Introduction

The large-scale utilization of phosphogypsum (PG), a by-product generated from the phosphorus fertilizer industry (phosphoric acid production), solves the waste disposal and pollution problems that cause severe pollution of the soil, water, and atmosphere[1]. Efforts have been made to use virgin and calcined PG as the retarders [2] in Portland cement (PC), but the hydration kinetics of PC are negatively affected compared to natural gypsum due to impurities [3].Therefore, the raw PG with a processing method such as calcining, lime water washing or neutralization through studies is strongly recommended [4]. To improve the performance of PG production, alkali-activated cements such as granulated slag, fly ash and zeolitic waste have been added to make PG-based cementitious binders [5], which have become a viable ecological alternative to traditional cementitious materials [6].

PG is widely used in ordinary Portland cement, oilwell cement, calcium sulfoaluminate cement [7], magnesium phosphate cement [8], alkali-activated fly ash [9], supersulfated cement [10], and cemented paste backfill [11]. Calcium sulfoaluminate (CSA) cement, which was developed by the China Building Materials Academy in the 1970s, was advertised as a sustainable alternative to PC. Belite sulfoaluminate (BSA) cement [11], which is based on CSA cement, is made from clinker containing 40–70% of C_2S and 20–50% of C_4A_3S. In this work, PG is used as a substitute for natural gypsum in the production of BSA cement and an excess of PG is added to the raw materials, which not only for the sulfur emissions, but also means that the anhydrite phase remains in the clinkers produced.

Preprints (www.preprints.org) | NOT PEER-REVIEWED | Posted: 30 May 2022 doi:10.20944/preprints202205.0401.v1

To the best of our knowledge, while the connections between the hydration process, mechanical strength, and calorimetry in relation to the cement compositions have been identified in previous [13], each investigation traced them back to a single phase and the main limitations are the absence of a standard phase composition and published data about composition-processing-performance relationships. In addition, as calorimetric studies on PG efficiency as a source of alkali-activated cements have shown [14], its interpretation cannot automatically be applied to these cements due to hydration processes.

For this reason and based on prior comments, the aim of this research was to analyze the chemical interaction among the solid phases, solid solution phases and aqueous solution in the process of the ternary cementitious system through the experimental tests and the GEMS software.

The morphology of hydration products, mechanical parameters and microscopic features such as crystal structure were characterized. The thermodynamic model was constructed to reveal the optimization and hydration mechanism of phosphogypsum ecological cement at a mesoscale.

2. Materials and methodology

2.1. Materials, mix composition and specimen preparation

2.1.1. Properties of materials:

Phosphogypsum (PG), fly ash (FA) and portland cement (PC) are utilized to prepare the phosphogypsum-based composite cementitious materials (PBM) in this study. The PG was excavated from the surface layer of a storage site, which belongs to a phosphogypsum tailings pond in Hubei province (China) and the FA was manufactured from Ezhou Power Plant Group (China). The mean humidity of raw PG obtained from six samples was 56.7%. The PC (M 42.5 OPC, Chinese National Standard, GB 175-2007) was brought from Huaxin Cement Co., Ltd, which the mineralogical compositions that was obtained from an X-ray diffraction (XRD) analysis are as follows: alite (C_3S, 40.65%), belite (C_2S, 34.52%), calclum aluminate (C_3A, 10.87%) and ferrite (C_4AF, 9.78%). The chemical composition of PG, FA and PC was investigated by the means of X-ray fluorescence spectroscopy (XRF) and the results have been presented in Table 1. Chemical characterization of raw materials was shown in Figure 1. Moreover, the physical properties of PG, FA and PC raw materials were shown in table S1. Ordinary tap water (TW) was used to mix the raw materials.

Table 1. XRF results of PG, FA and OPC in oxide weight percentage.

Sample	SO_3	CaO	SiO_2	P_2O_5	Al_2O_3	MgO	Fe_2O_3	TiO_2	LOI	SSA[1]
PG[2]	47.39	32.44	7.61	1.02	0.66	0.38	0.31	0.09	2.16	0.349
FA	0.1	2.45	54.15	0.33	32.25	2.79	4.26	1.02	0.06	0.737
PC	1.92	61.41	21.74	0.16	6.19	2.23	3.2	0.39	0.95	1.280

Note: SSA[1]: Specific surface area / ($m^2 \bullet g^{-1}$); PG[2]: Table S2 reports the chemical composition of PG obtained from the XRD quantitative analysis and XRF quantification.

Hemihydrate gypsum (HG) (β-$CaSO_4 \bullet 1/2H_2O$, purity≥97.0%) was obtained from Acros Organics, Germany and dihydrate gypsum (DG) ($CaSO_4 \bullet 2H_2O$, purity≥99.0%) was purchased from Sinopharm Chemical Reagent Co. Ltd., China. A polycarboxylate ether-based superplasticizer (PES) that met the ASTM C 494/C 499 M requirements for Type A water-reducing and Type F high-range water-reducing admixtures was employed as the admixture to prepare the high strength of composite cementitious materials.

Preprints (www.preprints.org) | NOT PEER-REVIEWED | Posted: 30 May 2022 doi:10.20944/preprints202205.0401.v1

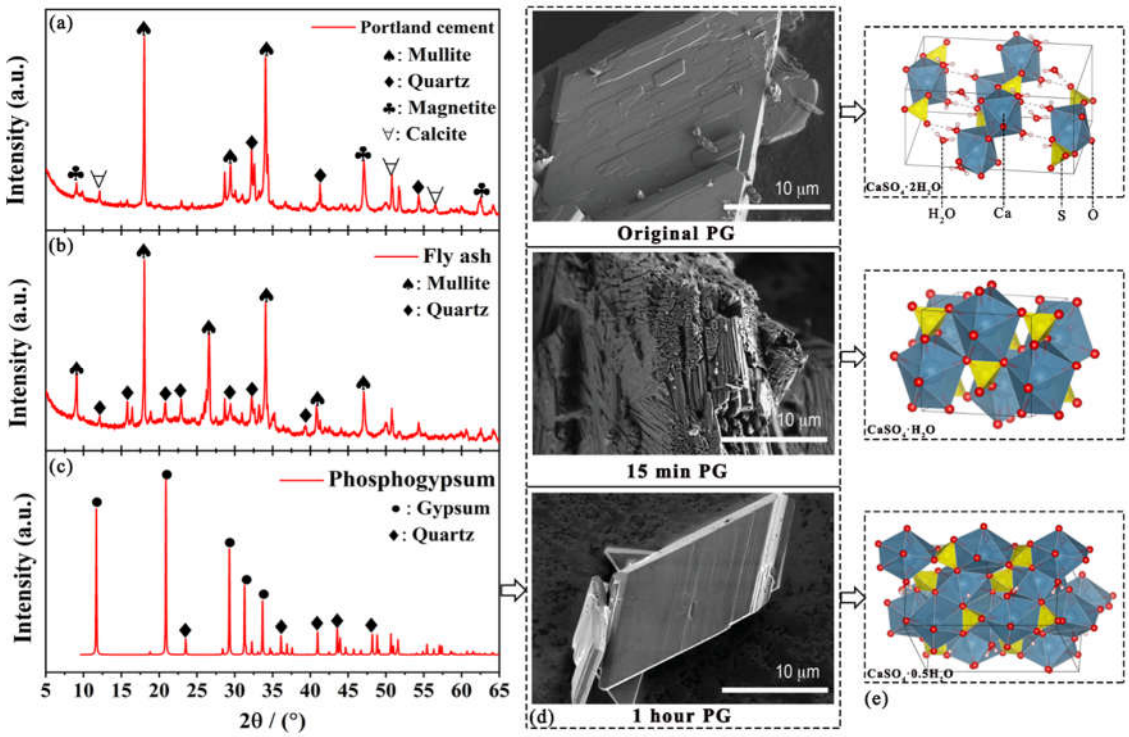

Figure 1. Chemical characterization of raw materials. (a)-(c): XRD patterns of PC, FA and PG; (d): SEM micrographs of changing in PG microstructure were taken of samples irradiated for the specified duration: Original PG, 15 min and 1 hour conventional heating at 100 ℃; (e): The crystal structure of the three observed phases are presented, structures were visualized using the VESTA software 45.

2.1.2. Mix composition:

In order to investigated the influence of the impurities in PG, curing time and conditions, dosage of PES, and PC, FA and solids contents on the strength of the PBM materials, three rounds of orthogonal experiments were designed by preparing different PC (1st test), PC+FA (2nd test) and PC+PES (3rd test) specimens with the use of different calcium sources (HG and DG), cementitious materials contents (80%, 61% and 19% by weight), percentages of PES (0%, 0.91%, 0.95%, 0.98% and 1.03% by weight) on two curing conditions (dry chamber and mosit curing). The water to solid ratio (W/S) and water to cement ratio (W/C) used were equal to 1:3 and 1:1 respectively. The summary of orthogonal experiments about mix composition of specimens is presented in Table 2.

Preprints (www.preprints.org) | NOT PEER-REVIEWED | Posted: 30 May 2022 doi:10.20944/preprints202205.0401.v1

Table 2. Summary of mix composition of specimens used.

Combination	Notation	PC	FA	HG	DG	PG	PES	W/S[1]	W/C[2]	Curing conditions	
		[%]	[%]	[%]	[%]	[%]	[%]	1:3	1:1	Dry[3]	Mosit[4]
PC	**1st test**	100	---	---	---	---	---	---	✓	---	✓
PC+HG	PH	80	---	20	---	---	---	✓	✓	---	✓
PC+DG	PD	80	---	---	20	---	---	✓	✓	---	✓
PC+PG	PP	80	---	---	---	20	---	✓	✓	---	✓
PC+FA	**2nd test**	61	19	---	---	---	---	✓	✓	✓	✓
PC+FA+HG	PFH	61	19	20	---	---	---	✓	✓	✓	✓
PC+FA+DG	PFD	61	19	---	20	---	---	✓	✓	✓	✓
PC+FA+PG	PFP	61	19	---	---	20	---	✓	✓	✓	✓
PC+PES	**3rd test**	73.49	---	---	---	---	0.90	---	✓	✓	---
PC+FA+PG	ECP-1	73.49	8.25	---	---	18.26	1.03	✓	✓	✓	---
PC+FA+PG	ECP-2	73.49	11.66	---	---	14.85	0.98	✓	✓	✓	---
PC+FA+PG	ECP-3	73.49	14.85	---	---	11.66	0.95	✓	✓	---	✓
PC+FA+PG	ECP-4	73.49	18.26	---	---	8.25	0.91	✓	✓	---	✓

Note:PC:Portland cement; FA: Fly ash; HG: Hemihydrate gypsum; DG: Dihydrate gypsum; PG: Phosphogypsum; PES: Polycarboxylate ether-based supperplasticizer; W/S[1]: water-to-solid ratio; W/C[2]: water-to-cement ratio; Dry[3]: Dry chamber [T=60±2°C, Water≤5%]; Mosit[4]: Mosit curing [T=20±1°C, Water≥95%]

2.1.3. Specimen perparation:

Firstly, five raw materials (PC, FA, HG, DG, PG, PES) were weighted by an electronic scale with an accuracy of 0.01 g and then mixed with TW accroding to the proportioning scheme until the slurry was fully dispersed. Secondly, the slurry was poured into a standard triple moulds with the dimension of 70.7 mm×70.7 mm×70.7 mm, then placed in a curing box, which the temperature and humidity were set as dry chamber (T=60±2℃, Water≤5%) and mosit curing (T=20±1℃, Water≥95%) respectively to the predetermined age of 3, 7, 28, 90, and 180 days. All the samples were divided into two groups. One group of these PBM materials was tested for the compressive strengths. Another group of these samples was dried using a vacuum drying oven to a constant mass, and then crushed and collected for the characterization of morphology and pore size distribution. The entire process of the PBM materials specimens preparation is shown in Figure 2.

Preprints (www.preprints.org) | NOT PEER-REVIEWED | Posted: 30 May 2022 doi:10.20944/preprints202205.0401.v1

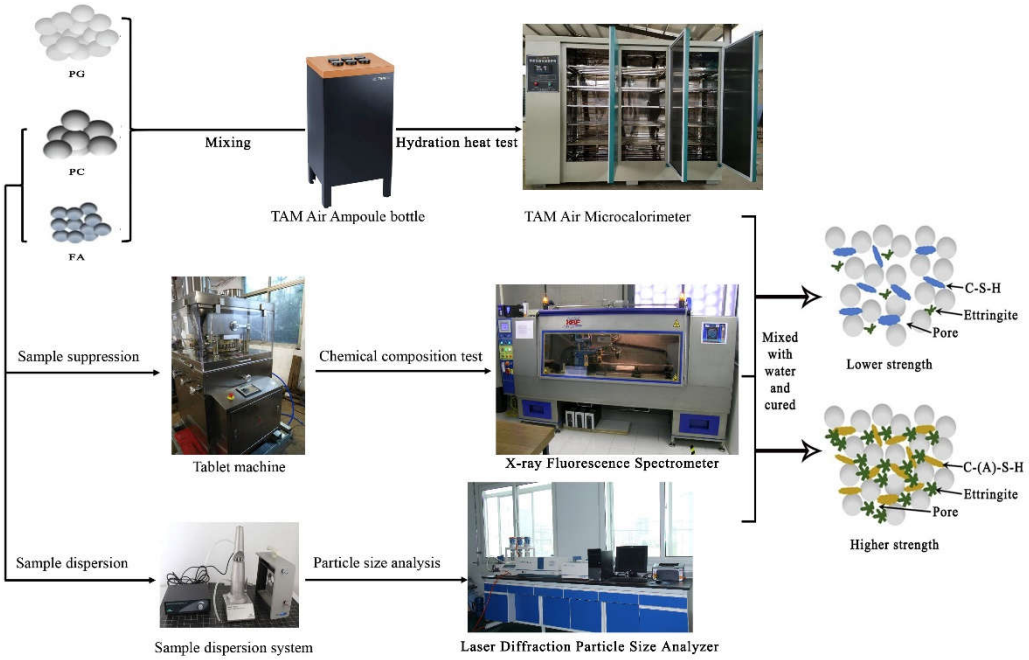

Figure 2. Schematic reaction diagram of PBM materials specimens.

2.2. Methodology

2.2.1. Experimental test methods:

For cement is a multiphase material, the chemical reaction of PBM materials is more complicated. It is necessary to start with a single-phase reaction, and then gradually improve to multi-phases reaction based on different degrees of simplification and assumptions. The main experimental research carried out in this study includes macroscopic and microscopic experimental test methods, which provides data support for calculating the contents of hydration products and hydration mechanism. The main experimental methods and sofrwares used were shown in Table 3, for more details, seen support materials S2.

 doi:10.20944/preprints202205.0401.v1

Table 3. Summary of experimental methods and softwares.

Experimental method	Logogram	Types	Softwares
Particle Size Distribution	PSD	BT-9300HT, China	Origin 2021
Uniaxial compressive strength	UCS	HY400X125 according to GB/T 17671-1999	Materials Studio
Mercury intrusion porosimetry	MIP	Micromeritics-9310 MIP device, maximum and minimum applied pressure of 100 MPa and 0.2 MPa	LAMMPS 19.0
Isothermal calorimetry	TA	An eight channel Thermal Activity Monitor (TAM) Air calorimeter	Visio 2021
Scanning Electron Microscopy	SEM	Zeiss EVO18, Carl Zeiss AG, Oberkochen, Germany	MDI Jade
X-ray fluorescence	XRF	PANalytical AXIOS spectrometer	VESTA
X-ray diffraction	XRD	X-Pert PRO DY2198 XRD, QXRD of Topas 4.2, Bruker AXS	Photoshop
Thermogravimetric-differential thermal analysis	TG-DTG	Mettler TGA/DSC 250 analyzer	GEM-selektor
Fourier Transform Infrared Spectroscopy	FTIR	PerkinElmer FTIR Spectrometer	
Nuclear magnetic resonance spectroscopy	NMR	^{29}Si and ^{27}Al solid-state MAS NMR	

2.2.2. Thermodynamic modeling:

Thermodynamic calculations were carried out using a geochemical software GEM-Selektor v.3 (GEMS) based on the Gibbs free energy minimization theory [15], and the thermodynamic properties of the aqueous complexes come from the cement database Cemdata 18 and Thermochimie database [16], which qualitatively computes equilibrium phase assemblages and speciation in complex hydration processes. The databases of thermodynamic data for common cement minerals like ettringite (AFt) and AFm phases, hydrotalcite, portlandite and calcium silicate hydrate (C-S-H phases), and solubility products of solids relevant for cementitious systems were selected to model PBM hydrate reaction. For lacking of approprite thermodynamic data of more phases, some hydration products such as the fluoride and phosphorus residues were computed and simulated as hydrogen fluoride (HF), fluorite and phosphoric acid, where the parameters were set at 0.1 MPa and 298.15K.

Preprints (www.preprints.org) | NOT PEER-REVIEWED | Posted: 30 May 2022 doi:10.20944/preprints202205.0401.v1

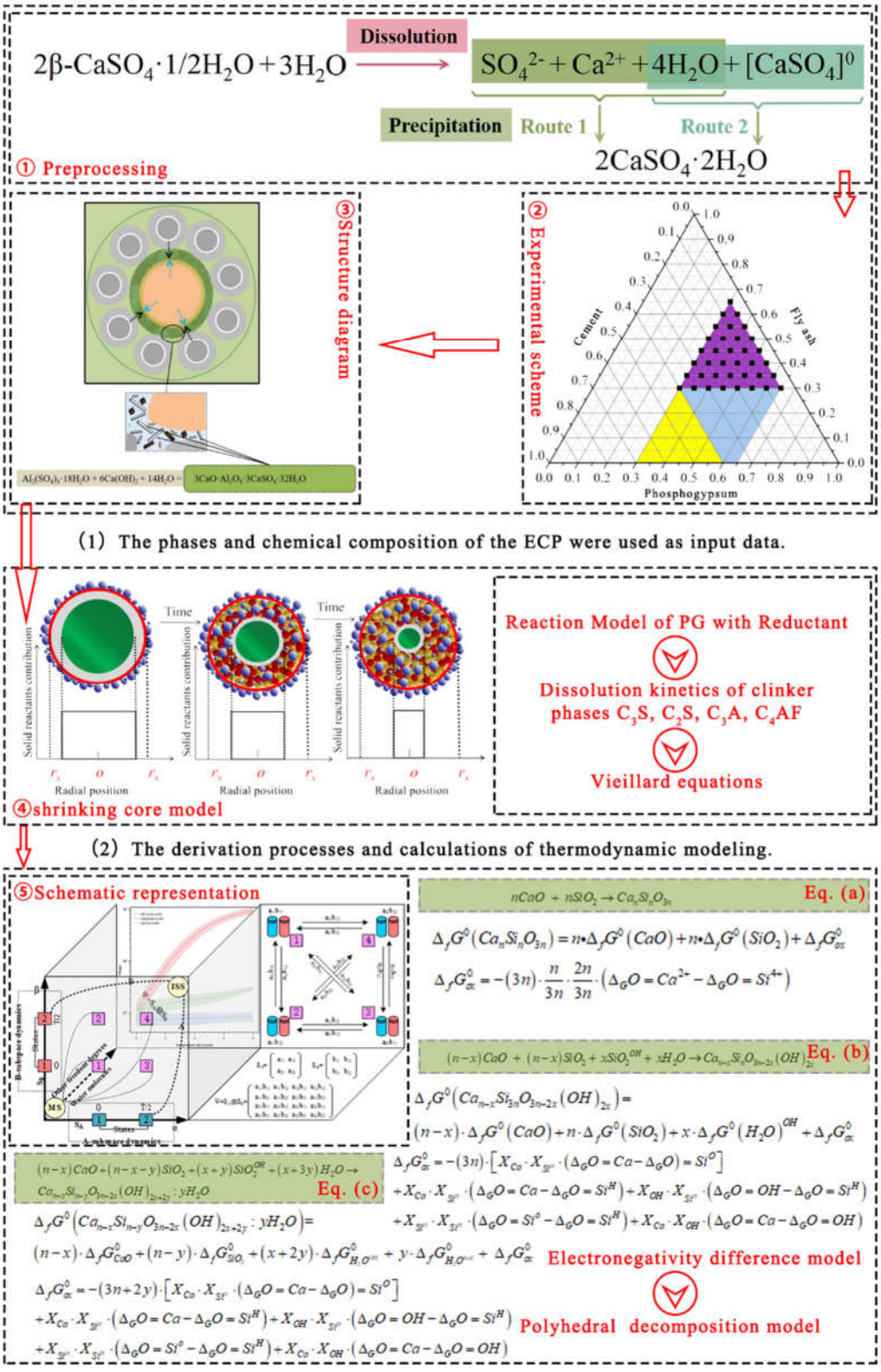

Figure 3. Schematic representation of the derivation processes and calculations of thermodynamic modeling.

The process of model represented in Figure 3 is composed of two parts, the electronegativity model for $\Delta_f G^0$ and the polyhedral model for S^0, Cp and V. For the electronegativity based part, seven unknowns $\Delta_G O{=}Ca$, $\Delta_G O{=}Ca^{ext}$, $\Delta_G O{=}Si^O$, $\Delta_G O{=}Si^H$, $\Delta_G O{=}Al$, $\Delta_G O{=}H_2O^{OH}$ and $\Delta_G O{=}H_2O_{hyd}$ are determined by minimization of the squared difference between the $\Delta_f G^0$ calculated for each mineral and the experimental values. For the

Preprints (www.preprints.org) | NOT PEER-REVIEWED | Posted: 30 May 2022 doi:10.20944/preprints202205.0401.v1

polyhedral part, six unknowns are refined by minimization of the squared differences between observed and calculated values, for each property [17]. The results of the model refinements are reported in Table 4.

Table 4. Properties of polyhedral model component oxides ($\Delta_f G^\circ$, S°, Cp and V) refined in this work.

Component oxides	$\Delta_f G°$	$\Delta_G O$	S°	C*p*	V°
	[kJ/mol]	[kJ/mol]	[J/mol·K]	[J/mol·K]	[cm³/mol]
CaO	-603.30	303.60	43.80	47.99	16.52
CaO_{ext}	-603.30	464.23	---	---	---
SiO_2	-856.28	221.31	56.41	62.16	30.28
SiO_2^H	-856.28	323.81	---	---	---
H_2O_{OH}	-187.50	187.50	7.05	-13.33	-1.93
H_2O_{hyd}	-221.47	221.47	47.95	43.56	13.96

3. Results and disscussion

3.1. Experimental results

3.1.1. Uniaxial compressive strength:

Table 5 presents the strengths of specimen up to 180 days at diffetent curing condition. This study illustrated that PBM cured under different curing conditions had different technical properties. PBM cured under mosite curing conditions was found to achieve higher compressive strength values than those cured under dry chamber conditions for all treatments and inclusion ratios. At 28 days, PBM has already evolved a certain strength, which is still comparatively low, as hydration is suppressed when the content of soluble phosphogypsum gradually decreases. In system ECP, the UCS of ECP-1 (58.6 MPa) and ECP-2 (76.9 MPa) were lower than the UCS of ECP-3 (85.7 MPa) and ECP-4 (92.1 MPa) that these were selected for XRD and mineralogical studies. This is probably because a considerable amount of calcium carbonate is formed after carbonization, which not only causes the volumn expansion but also leads to external strength. Combined with the observations from the UCS test, it can be commented that the early robustness of PBM with higher dissolved PG was poor. Besides, the PG affects the alkalinity of the solution [18], which is also detrimental to the development of ettringite, which leads to a lower early strength. Morevoer, at later stage, the C-S-H and C-A-H gels [19] are gradually carbonized, and converted into a gel with a high extent of polymerization, which generates the new capillary pores.

Table 5. Strengths (UCS/MPa) of specimen up to 180 days at different curing condition.

Specimen	3 days	7 days	28 days	90 days	180 days
PH	39.4	50.0	67.1	---	---
PD	36.6	45.9	61.0	---	---
PP	18.1	19.9	32.3	---	---
PFA	37.8	39.7	51.1	---	---
PFD	33.2	39.5	45.6	---	---
PFP	25.1	28.9	38.8	---	---
ECP-1	11.5	20.8	29.3	42.7	58.6
ECP-2	28.3	34.1	46.3	58.4	76.9
ECP-3	37.2	47.8	60.4	73.6	85.7
ECP-4	51.6	64.8	72.4	87.1	92.1

Preprints (www.preprints.org) | NOT PEER-REVIEWED | Posted: 30 May 2022 doi:10.20944/preprints202205.0401.v1

3.1.2. XRD analysis:

In the microstructure characterization of PBM, minerals and hydration products are the two main phases that are intensively investigated. Figure 4 presents the XRD analysis patterns of the hydration products of the ECP-1, 2, 3, and 4 at the age of 3, 7, and 28 days, that the spectral lines of the hydration products were mainly dispersed peaks, and the phases mainly included OH, C_2S, C_3S, C_4AF, C_3A and unhydrated mineral admixture phases. A selection of X-rays patterns between 10º and 20º (2θ) for hydrated ECP is plotted that the characteristic peak of calcium silicate hydrate (C-S-H) appeared between 12°~13°. There was a dispersion peak in the range of 2θ from 14° to 16°, which was more obvious at 3 days and 7 days, indicating that the intensity of the diffraction peaks of C_2S, C_3S and mineral admixture phase components decreases continuously with the prolongation of reaction time, that is the composite cementitious materials are continuously hydrated to form AFt crystals during curing period. According to the study [20], when a large amount of minerals existed, a variety of ions would replace each other to form complex compounds. Due to the continuous dissolution and hydration of phosphogypsum calcium ions, there will be a small amount of OH^- and CH phase appears, the crystallinity of CH generated by hydration is relatively poor. As the reaction progresses, it will be absorbed with cement hydration products, making it difficult for CH to reach saturation, so the diffraction peak of CH is relatively weak and inconspicuous at 28 days.

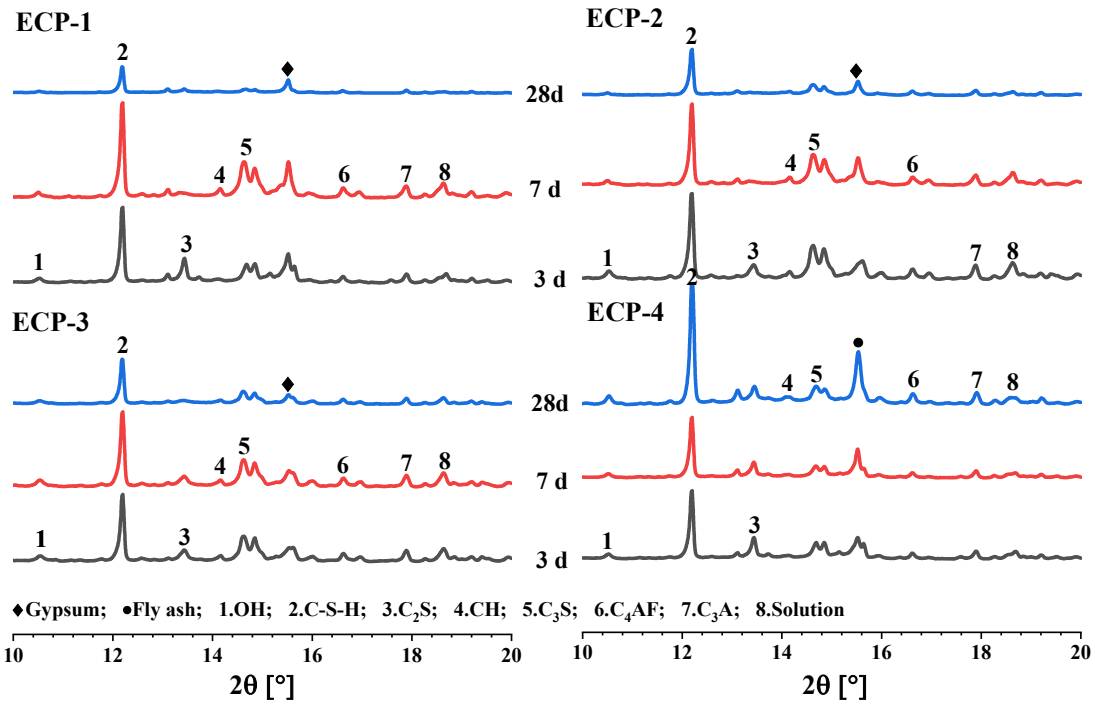

Figure 4. Laboratory X-ray powder diffraction patterns of hydration products for pastes.

3.1.3. TG-DTG analysis:

Figure 5 shows the TG-DTG curves of ECP samples hydrated. It can be seen from Figure 5 that the hydration reaction at the age of 28 days contains three endothermic peaks and one exothermic peak: (1) The 1st peak between 98℃ and 102℃ was the endothermic peak of the dehydration of C-S-H gels and AFt crystals, and the corresponding TG curve showed that the mass loss at this stage was 4%~5%. (2) The 2nd peak between 420℃ and 440℃ was the endothermic peak when PG was dehydrated and transformed into gypsum, and the corresponding TG curve showed that the mass loss at this stage was 1%~2%. (3) The 3rd peak between 660℃ and 680℃ was the endothermic peak of the physical filling of the FA effect which has not been activated and the characteristic transformation of C_2S in cement. The corresponding TG curve showed that the mass loss at this stage was

Preprints (www.preprints.org) | NOT PEER-REVIEWED | Posted: 30 May 2022 doi:10.20944/preprints202205.0401.v1

2%-3%. (4) The exothermic peak between 750℃ and 770℃ indicated that the C-S-H gel transforms from colloidal to flocculent crystal, which is mainly caused by the transformation from AFt crystals to AFm crystals [21].

Compared with XRD analysis results, it can be seen that the endothermic peaks corresponding to AFt, C-S-H and CH increased with the increase of PG content, respectively. The addition of PG promotes the formation of ettringite (AFt) and the dissolution of C_3S, thereby accelerating the early hydration reaction of ECP. During the hydration process, almost all of the FA participated in the reaction, but there was still a small amount of unreacted PG. The main reason was that PG contains a small amount of soluble phosphorus containing impurities, which will react with the hydration product CH to form insoluble salt calcium phosphate, which impedes normal hydration of PG and C_3A. At the same time, mass loss of specimen between 98℃ and 102℃ indicated that hydration of hardened slurry was still undergoing hydration at 28 days, and its hydration products increased continuously, ensuring the continuous growth of ECP strength.

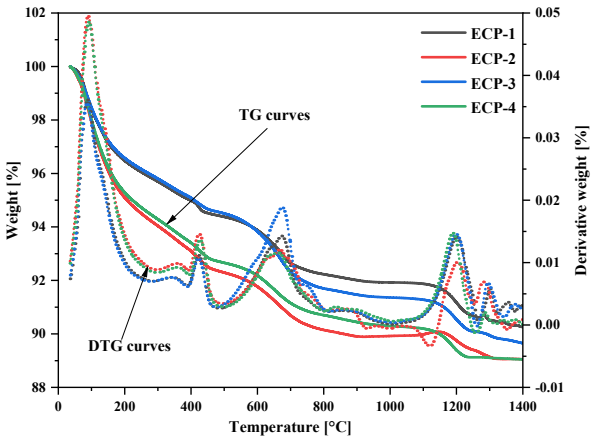

Figure 5. TG-DTG curves of ECP samples hydrated. .

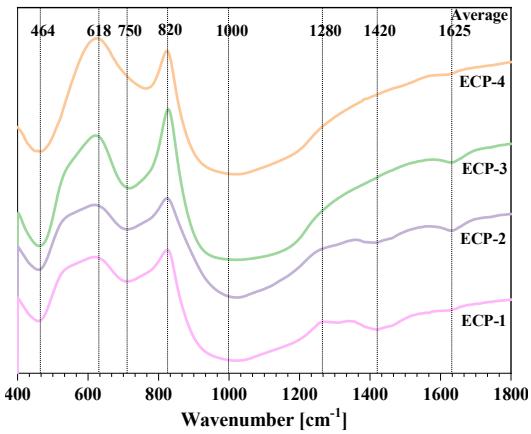

Figure 6. FTIR for hydrated pastes for ECP samples at 28 days.

3.1.4. FTIR analysis:

The FRIR spectra of ECP-1, 2, 3 and 4 at the age of 28 days are shown in Figure 6. The bending vibration peaks at 750 cm^{-1} and 464 cm^{-1} indicated asymmetric stretching of Si-O bonds in $[SiO_4]^{2-}$ion in C_2S and symmetric stretching of Si-Si bonds in C-S-H gels. The characteristic peak at 820 cm^{-1} and 618 cm^{-1} showed the asymmetric stretching vibration bands of Al-O-Si bond, which are related to the asymmetric elongation of $[AlO_4]^{5-}$ ions in aluminates and aluminosilicates (C-A-H and C-A-S-H), and reflects the polymerization of silicon-oxygen tetrahedra in C-S-H gels. It makes up for the deficiency that it is not easy to detect floccule C-S-H gels by XRD. The asymmetric stretching vibration band belong to

Preprints (www.preprints.org) | NOT PEER-REVIEWED | Posted: 30 May 2022 doi:10.20944/preprints202205.0401.v1

the medium C-O bond of $[CO_3]^{2-}$ at 1000 cm^{-1} indicated the formation of amorphous or low-crystalline carbonate, which was related to the existence of semi-aluminate and single-carbon aluminate phases. The bands at 1420 cm^{-1} and 1280 cm^{-1} showed the stretching and bending of O-H bond in water molecules, indicating that with the continuous hydration reaction, the number of hydration products gradually increased, and the hydroxyl content in the system also increased. There was a weak absorption peak at 1625 cm^{-1}, indicating a stretching vibration band of calcium hydroxide (CH), which is consistent with the XRD results. According to FTIR results, the hydration products at the age of 28 days were mainly AFt, silicate and calcite, C-S-H gels with low crystallinity and carbonate phases.

3.1.5 ^{29}Si MAS-NMR analysis:

The ^{29}Si MAS-NMR spectrum of the deconvolution of signals for ECP during 28 days is shown in Figure 7. It can be seen from the Figure 7 that there was Q^1 spectral signal at -79 ppm and -85 ppm, which is related to the end unit of silicon chain, there was $Q^2(1Al)$ spectral signal at -82 ppm, which represents the Al ionic bond contained in the adjacent tetrahedron. The Q^2 spectrum signal at -85 ppm indicated that C-S-H was generated in hydration products. Its larger spectral intensity indicates that a larger average silicon chain was required to synthesize C-S-H. To sum up, the increase of PG content can accelerate the dissolution of C_3S, the polymerization and transformation of C-S-H gel, which can partially convert C-S-H gels to more dense C-A-S-H gels.

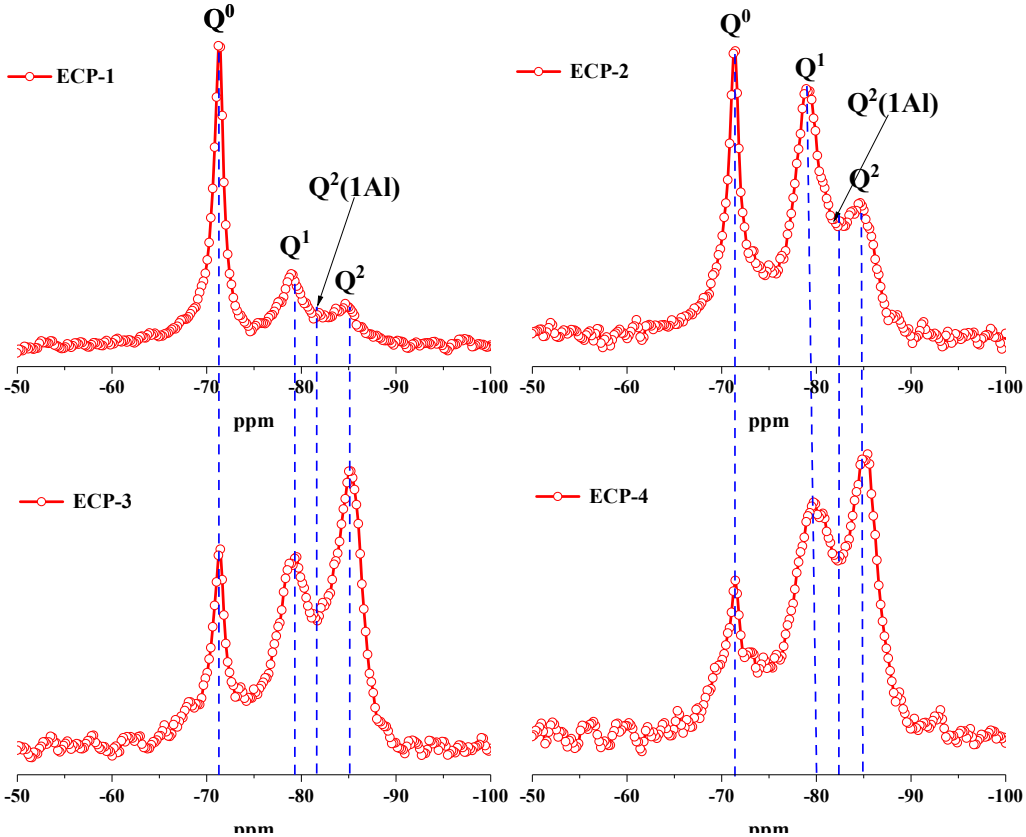

Figure 7. ^{29}Si MAS-NMR spectra showing the deconvolution of signals for ECP during 28days.

Figure 8 shows the ^{29}Si NMR spectra of the composites with different Ca/Si ratios. It can be seen from Figure 8 that ^{29}Si NMR spectrum has three main peaks at -78 ppm, -81 ppm and -85 ppm, corresponding to the sites of Q^1, $Q_P^2(1Al^{IV})$ and Q^2 in the silicon chain (Dreuerketten structure), grafted on both sides of CaO_2 layer respectively. The difference of these sites was mainly related to Ca/Si ratios and pH values in the environment. In addition, the resonance of Q^2 is mainly affected by paired Q_P^2 and bridging site Q_b^2, with

Preprints (www.preprints.org) | NOT PEER-REVIEWED | Posted: 30 May 2022 doi:10.20944/preprints202205.0401.v1

resonance frequencies of -85 ppm and -83 ppm, respectively. At the same time, the chemical shift of ^{29}Si NMR spectrum was affected by the degree of polymerization of silicon-oxygen tetrahedron. With the increasing of Ca/Si ratios, the chemical shift of ^{29}Si gradually moved to the right, indicating that the binary hydrate was decreasing and the monomeric Si tetrahedra was increasing in the hydration reaction.

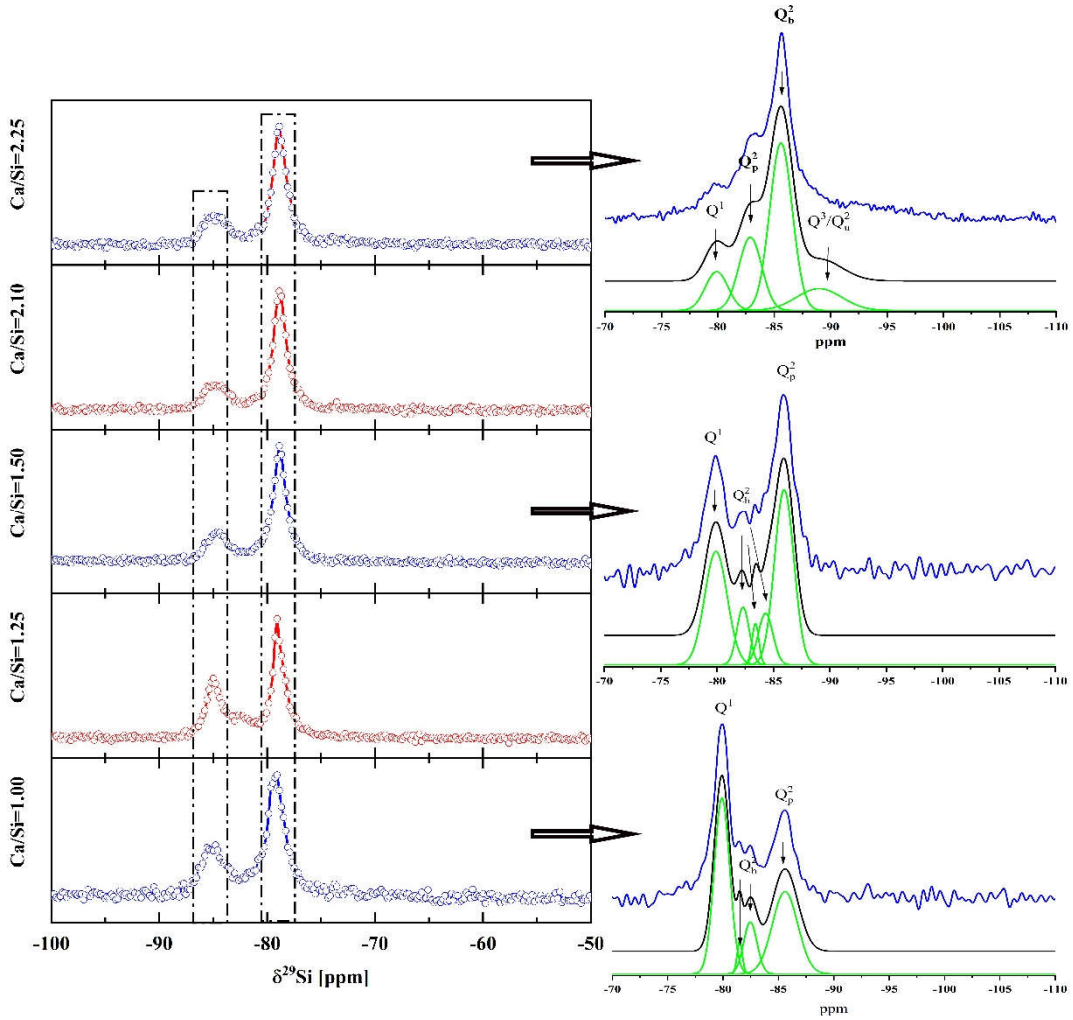

Figure 8. ^{29}Si NMR spectra of different Ca/Si ratios.

3.2. Thermodynamic analysis

3.2.1. Thermodynamic parameters determination

The thermodynamic parameters of cement mineral phase are given in Table 6. The hydration products are mainly divided into calcium silicate hydrate (C-S-H), $Ca(OH)_2$(CH), ettringite (AFt) and single sulfur calcium aluminate hydrate (AFm), among which the hydration of C_3S, C_2S and C_4AF will generate CH. The corresponding hydration dynamics equation and heat balance coefficient are shown in Table 7. Studies have shown that the amount of CH generated by the complete hydration of 1mol C_3S was more than 1.3mol. Meanwhile, since two pozzolanic reactions occured during the hydration process of FA, CH as a product of the early hydration process usually reacted with the SiO_2 generated in the slurry. Thus, two types of calcium silicate hydrate phase, type C-S-H_1 and type C-S-H_2 were generated.

Preprints (www.preprints.org) | NOT PEER-REVIEWED | Posted: 30 May 2022 doi:10.20944/preprints202205.0401.v1

Table 6. The thermodynamic database of PC's hydration phases.

Species parameters		C_3S	C-S-H-jen	Portlandite	$H_2O(l)$
$\Delta_f H°$	kJ/mol	-2931	-2723	-985	-286
$\Delta_f G°$	kJ/mol	-2784.33	-2480.81	-897.01	-237.18
V_m	$10^{-6}m^3$/mol	72.4	106*	33.1	18.1
M	kg/mol	0.22833	0.19132	0.07409	0.01802

*Note: The molar volume of CSH is calculated according to chemical formula $C_{1.67}SH_4$ instead of $C_{1.67}SH_{2.1}$ since the early age's CSH is under 100% relative humidity.

Table 7. Equations of hydration kinetics of ECP hydration products.

Phases	Formula	log K*so*
AFt	$Ca_6Al_2(SO_4)_3(OH)_{12}\bullet 26H_2O \rightarrow 2Al(OH)_4^- + 6Ca^{2+} + 26H_2O + 4OH^- + 3SO_4^{2-}$	-44.9
AFm	$Ca_4Al_2(SO_4)(OH)_{12}\bullet 6H_2O \rightarrow 2Al(OH)_4^- + 4Ca^{2+} + 6H_2O + 4OH^- + SO_4^{2-}$	-29.26
CH	$Ca(OH)_2 \rightarrow Ca^{2+} + 2OH^-$	-5.2
C-S-H_1	$Ca^{2+} + SiO_3^{2-} \rightarrow CaSiO_3^O$	2.9
C-S-H_2	$Ca^{2+} + HSiO_3^{2-} \rightarrow CaHSiO_3^+$	0.5
CsH_2	$CaSO_4\bullet 2H_2O \rightarrow Ca^{2+} + SO_4^{2-} + 2H_2O$	-4.581
$CsH_{0.5}$	$CaSO_4\bullet 0.5H_2O \rightarrow Ca^{2+} + SO_4^{2-} + 0.5H_2O$	-3.59
Cs	$CaSO_4 \rightarrow Ca^{2+} + SO_4^{2-}$	-4.357
SiO_2	$SiO_2(quartz) \rightarrow SiO_2^O$	
CH[6]	$C_3S+5.3H \rightarrow C_{1.7}SH_4+1.3CH$ $C_2S+4.3H \rightarrow C_{1.7}SH_4+0.3CH$ $C_4AF+xC\bar{S}H_2+yH \rightarrow zC_mA\bar{S}H_n+CH+FH_3$	
C-S-H[7]	Calcium-silicates $+H_2O \rightarrow$ C-S-H_1 + $Ca(OH)_2$ $Ca(OH)_2$ + reactive $SiO_2 + H_2O \rightarrow$ C-S-H_2	

The hydration rate and hydration heat cumulative curves for ECP-1, 2, 3 and 4 are shown in Figure 9. It can be seen from Figure 8 that the total hydration reaction heat of ECP ranges from 400 J/g to 550 J/g, and the peak times of hydration rates of the four types of ECP are different. The peak value of hydration rate of ECP-1 and ECP-2 appeared early and changed rapidly and lasted for about 3 hours. The peak value of hydration rate of ECP-3 and ECP-4 appeared in the first hour, and in the later period, the hydration rate firstly decreased, then rose and finally reached stability. These results indicate that the early hydration of PG can significantly change the rate of hydration, while the continuous hydration of FA inhibits the increase of hydration rate to a certain extent, but does not affect the time when the hydration rate change reaches the extreme value. In addition to the brief initial exothermic peak at the beginning of hydration of ECP, the hydration exothermic curve also includes the exothermic peak generated by the dissolution of C_3S and the exothermic peak generated by the secondary dissolution of C_3A.

Preprints (www.preprints.org) | NOT PEER-REVIEWED | Posted: 30 May 2022 doi:10.20944/preprints202205.0401.v1

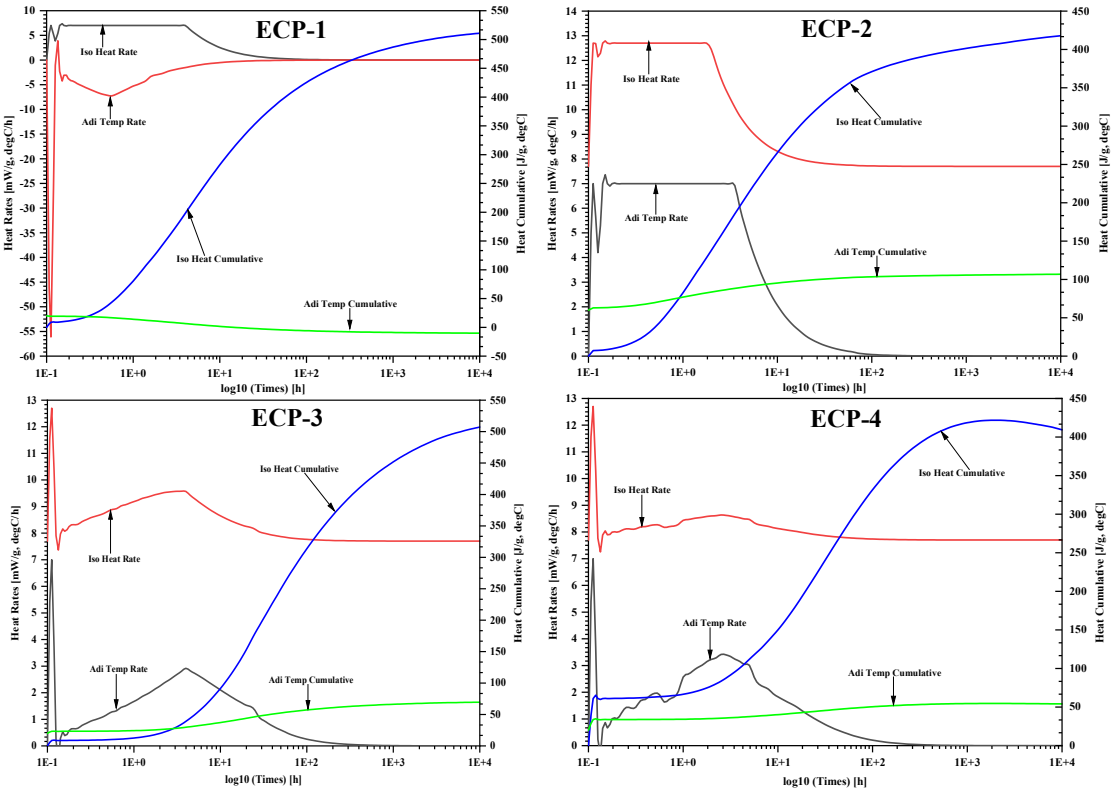

Figure 9. Hydration rate and hydration heat cumulative curves for ECP-1, 2, 3 and 4.

3.2.2. Simulation and calculation base on GEMS:

Phase evolution of hardened pastes under different curing conditions by the thermonamic simulation is shown in Figure 10. It can be seen from Figure 10 that CH and C-S-H gels in ECP hydration products were increasing with the continuous hydration, while C_3S and H_2O were decreasing. Up to the age of 28 days, C_3S and OH were still existed, indicating that the hydration reaction had not been completed. In test of ECP-1 and ECP-2, a little PG was participated in hydration in the early stage, but in the later stage of hydration, it was completely hydrated. In test of ECP-3 and ECP-4, there were some FA mineral phases existed in the later hydration stage, indicating that only part of PG dissolved and hydrated with C_3A and C_3S in cement in the early stage, and $[SiO_4]^{2-}$ and $[AlO_4]^{5-}$ networks in FA vitreous had not depolymerized yet, and mainly participated in the reaction by physical filling [22]. In the late hydration stage, the pozzolash activity of FA [23] was gradually activated and participated in the reaction, resulting in the existence of some FA at the age of 28 days.

Meanwhile, due to the interaction between sulfate ions and C_3S, the addition of PG delayed the initial hydration of C_3S, and the formation of gypsum had a promoting effect on the hydration of C_3S, mainly resulted of the changing of C-S-H morphology and the increasing of ionic strength, ettringite (AFt) crystals inhibited the formation of Al^{3+} ions in pore solution and enhanced the hydration mechanism of C_3S. Thus, a more complex sulfate equilibrium system was formed in the middle and late stages.

Preprints (www.preprints.org) | NOT PEER-REVIEWED | Posted: 30 May 2022 doi:10.20944/preprints202205.0401.v1

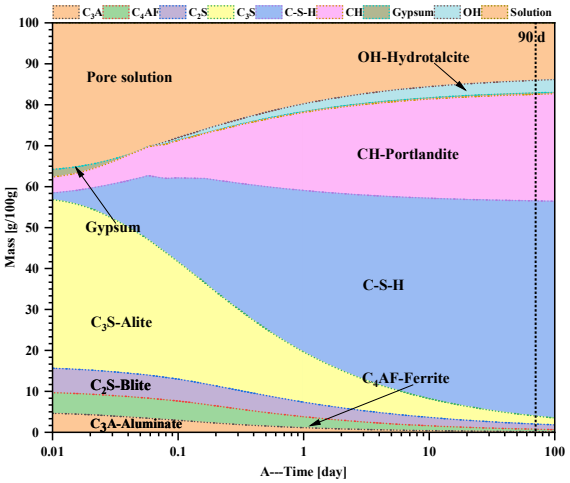

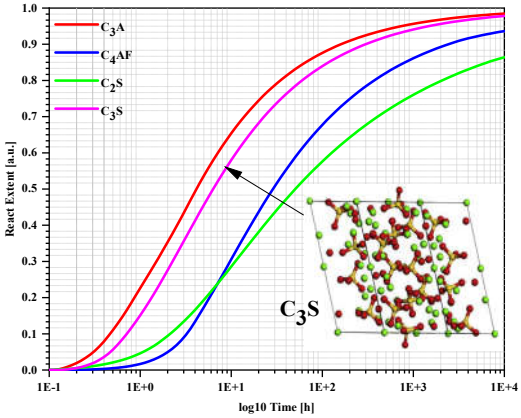

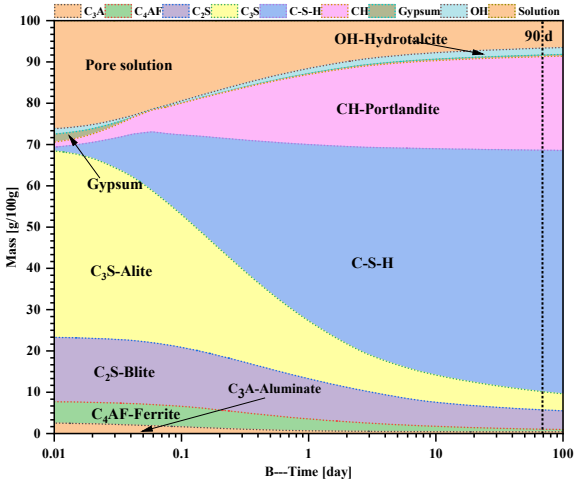

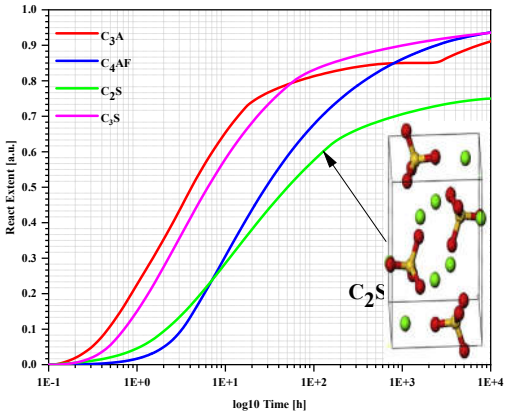

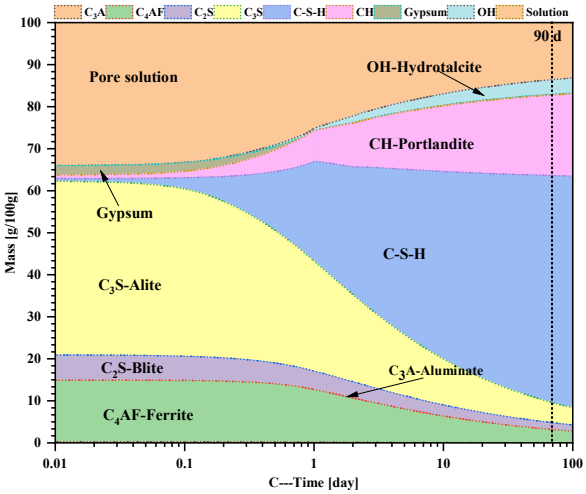

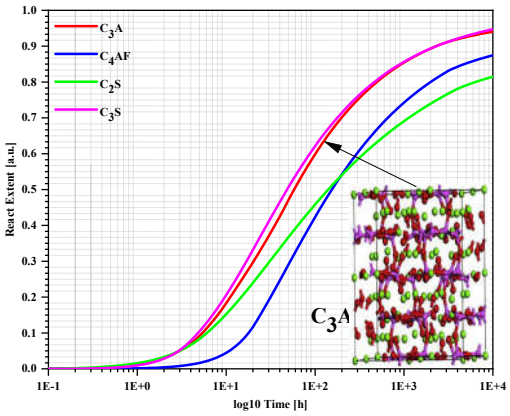

Preprints (www.preprints.org) | NOT PEER-REVIEWED | Posted: 30 May 2022 doi:10.20944/preprints202205.0401.v1

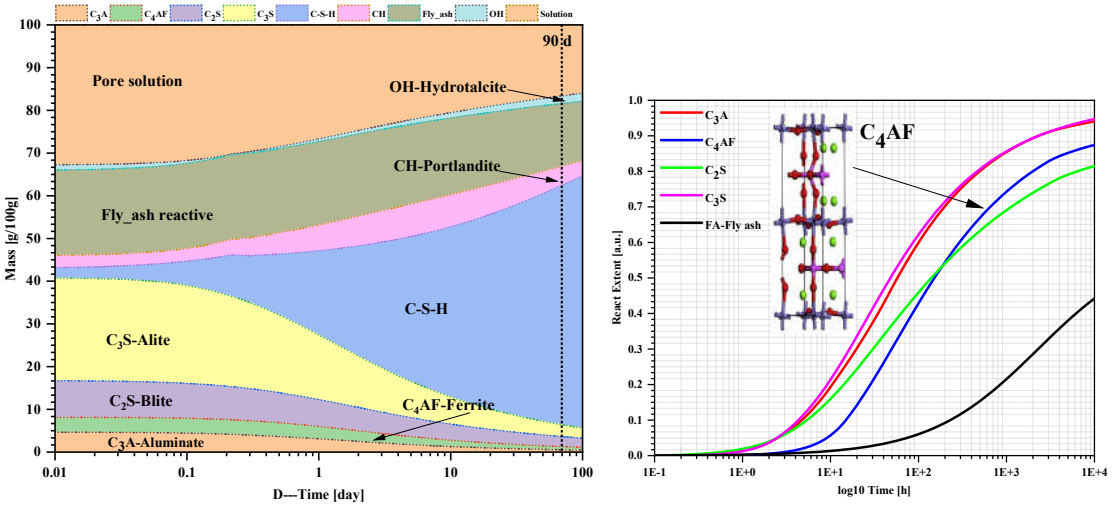

Figure 10. Phase evolution of hardened paste under different curing conditions by the thermodynamic simulation.

3.2.3. Thermodynamic property analysis:

The standard formation enthalpy $\Delta_G O$ and entropy S° of each reaction phase in ECP were used to calculate the $\Delta_f G°$ generated by the dissolution reaction of each major mineral phase in hydration products, according to the model derived from the Section 2.2.2. Since the solubility product of C-S-H gels are very small, and the surface state of silicate ion in hydration solution and hydroxylation degree of C_3S cannot be determined, and the dissolution of various mineral phases in hydration reaction has not reached equilibrium, in order to compare with the calculation results in literatures, In this paper, common chemical equations and calculation models were used to calculate the gel saturation index of C_3S and C-S-H. The thermodynamic models of C-S-H with Ca/Si ranging from 1.0 to 2.3 were constructed by NMR and other methods to demonstrate the possibility of polymorphic optimization in hydration products under different Ca/Si ratios, thereby explaining the correlation between C-S-H formation and C_3S and redecomposed ion groups during hydration reaction. Combined the thermodynamic model and data given by the above mentioned, the decomposition into consituent oxides for the minerals considered and solid solution moderls of C-S-H at the age of 28 days are summaried in Table 8.

Table 8. Decomposition into constituent oxides for the minerals considered and solid solution models of C-S-H.

Phases	Ca/Si	CaO	CaO_{ext}	SiO_2	SiO_2^H	H_2O_{OH}	H_2O_{hyd}	$\Delta_f G°$	$\Delta_G O$	S°	Cp	V°
Unit	---	%	%	%	%	%	%	kJ/mol	kJ/mol	J/mol·K	J/mol·K	cm^3/mol
$C_{1.25}S_{1.25}H_{2.5}$	1.0*	0.69	0.00	0.61	0.39	0.28	0.68	-2650.4	-2782.0	197.0	234.1	79
$C_{0.8}S_{0.7}H_{1.8}$	1.25	0.70	0.00	0.61	0.39	0.28	0.69	-1656.7	-1742.4	144.4	166.9	48
$C_{1.5}SH_{2.5}$	1.5	0.83	0.23	0.33	0.67	0.34	0.89	-2594.8	-2722.4	202.0	237.0	81
$C_{1.67}SH_{2.1}$	2.1	0.92	0.31	0.17	0.83	0.37	1.06	-2601.9	-2723.0	175.1	210.1	78
$C_{1.5}S_{0.7}H_{2.5}$	2.25	0.96	0.46	0.08	0.92	0.45	1.12	-2285.2	-2400.7	203.1	232.8	81

Preprints (www.preprints.org) | NOT PEER-REVIEWED | Posted: 30 May 2022 doi:10.20944/preprints202205.0401.v1

Figure 11 shows the variation of characteristic values of hydration kinetics parameter C-S-H oxide-solution model data with Ca/Si ratio in ECP. It can be seen from the Figure 11, the values of mineral single-phase CaO, SiO_2^H and H_2O_{hyd} in hydration products gradually increase with the increase of Ca/Si ratio, which indicates that when Ca/Si ratios were high or low, the maximum dissolution rate and dissolution amount of early cement and phosphogypsum increase, and the duration is different, but the hydration mechanism is not the same. At this time, with the continuous progress of the reaction, the values of CaO_{ext} and H_2O_{OH} are in a proportional relationship, mainly mainifested in the acidic environment formed by the early hydration of PG with water, which leads to the continuous dissolution of Ca^{2+} in the hydration solution and accelerates the ionization of H_2O. When the Ca/Si ratio was relatively high, the cement hydrated at the early stage, making the hydration environment weakly alkaline [22], which promoted the generation of phosphate hydration products such as PG and accelerated the consumption of hydration products in cement, thus promoting the acceleration of the ionization of H_2O. From the perspective of the entire hydration process of ECP, the dissolution process of PG, FA, PC, formation process of amorphous phase, and formation process of C_3S and C-S-H gels were proceed sequentially, but partially overlapping [23]. The emergence time of the former process and its influence on the latter process. When Ca/Si=2.25 in ECP, the formation process of amorphous phase like SiO_2 in FA was followed by the dissolution of PG that the time difference between the two processes was very small, which can be confirmed by Subgroup analysis. The formation process of amorphous phase during the formation of ECP hydration products was a key factor affecting the quantity and type of hydration products [24].

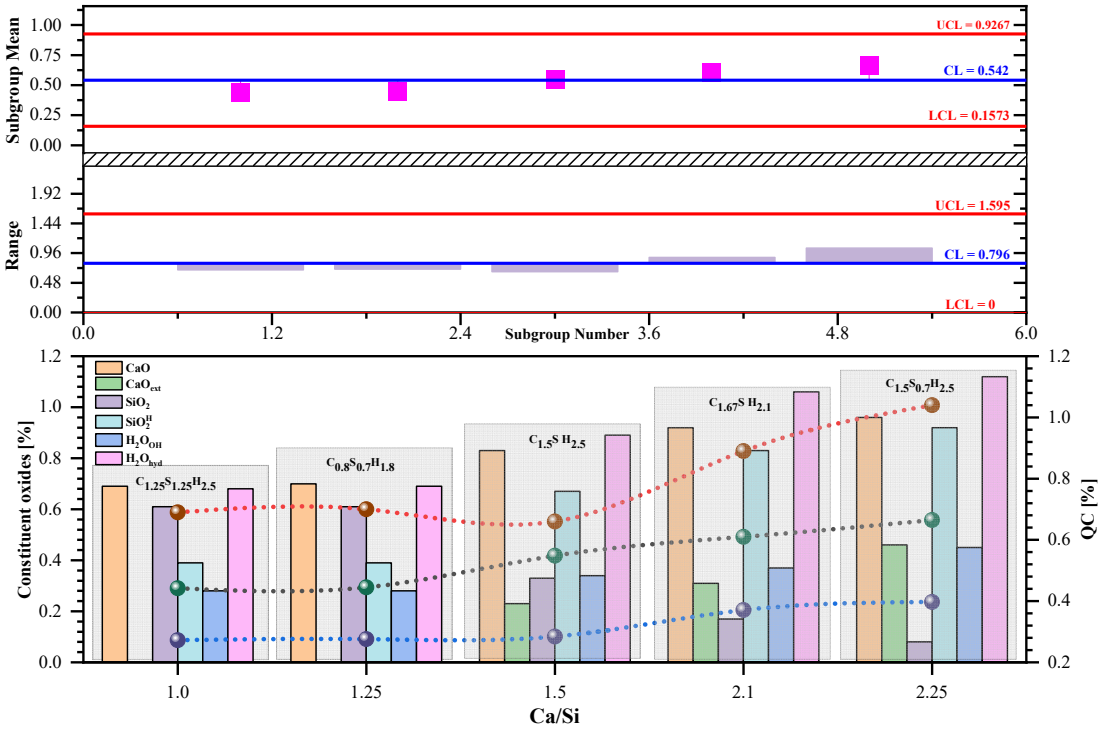

Figure 11. The changes of the characteristic values about constituent oxides at different Ca/Si ratio of C-S-H.

4. Evolution mechanism of hydration reaction

Figure 12 shows the ternary phase diagram of the main hydration products in the ECP system. The hydration reaction mechanism of various raw materials in ECP is mainly shown as follows: at the initial stage of the reaction, C_3A and C_4AF are the first to be hydrated. Calcium sulfate dihydrate reacts with CaO and Al_2O_3 to generate AFt needlelike crystals, which are connected with cement particles to form bridges. Subsequently, a large

Preprints (www.preprints.org) | NOT PEER-REVIEWED | Posted: 30 May 2022 doi:10.20944/preprints202205.0401.v1

amount of $Ca(OH)_2$ and low-density C-S-H gels were generated by hydration of C_3S and β-C_2S. Parts of CH were precipitated and filled in the crystal space structure formed by low-density C-S-H gel and PG particles. Finally, the low-density C-S-H gels were further hydrated to form plate-like high-density C-S-H and C-A-S-H gels.

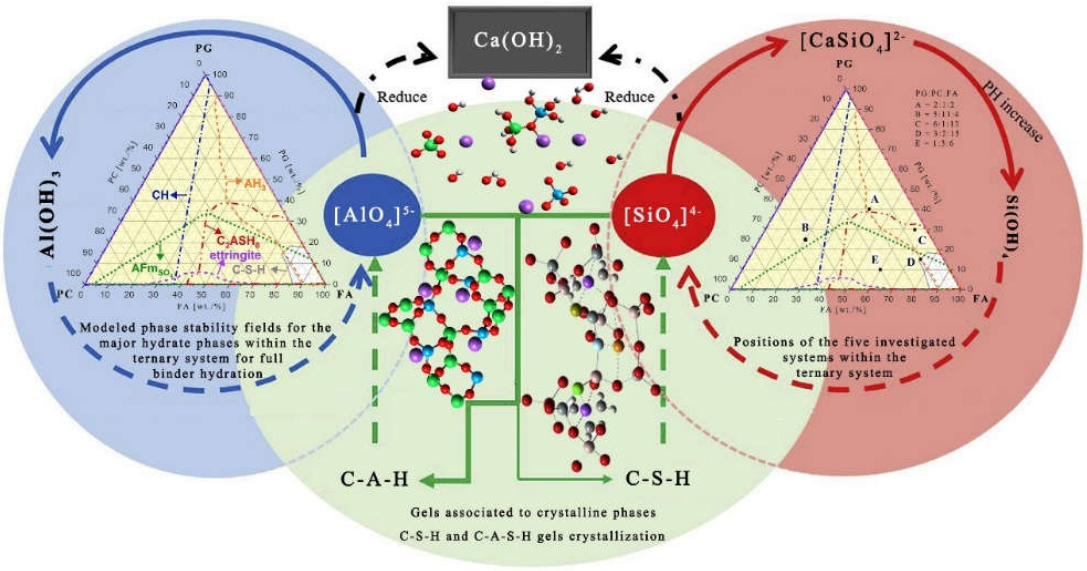

Figure 12. (Left) Modeled phase stability fields for the major hydrate phases within the ternary system for full binder hydration. (Right) Positions of the five investigated systems within the ternary system.

In accordance with the study, PBM is a three-phase composite material where hydration is the consequence of the co-hydration of multiple minerals. The nucleation process is a reaction that can mainly be described as a solid, liquid and gaseous phases that has passed through four stages, as demonstrated in Figure 13.

I: Physical and chemical mixing and modification treatment. PG, PC and FA are pulverized in a certain proportion to form a slurry and dissolved to provide a good hydration environment.

II: Modification and hydration with low calcium content. The hydration of three materials produces a plasma like $[SiO_4]^{2-}$, Ca^{2+}, $[AlO_4]^{5-}$, $[CaSiO_4]^{2-}$ and OH^- that breaks any chemical bond, reploymerizes to form new hydrates that are on the surface particles adhere to the solid, gradually forming an irregular surface layer and pore structure. This phasse manifests itself mainly that the ions of $[SiO_4]^{2-}$, dissolved by C_3S and C_2S, react with calcium aluminate to form AFt, and then combinated with Al_2O_3 and SiO_2, dissolved by FA, produce C-S-H gels, which be oiured into the ettringite framework. The growth of C-S-H, the product of hydration in this phase, occurs mainly on the surface of the mineral mud particle.

III: Secondary hydration. The hydration products react with free ions to gradually form C-S-H and irregular crystals that bridge each other to form a layer and network structure and then combine to form a new silicate framework. Part of the crystals and unreacted particles are filled into the framework and pore structure, which form a certain strength of materials. This phase manifests itself mainly in the fact that the vitreous structure of C_3A in the PC is stimulated to depolymerize by the $Ca(OH)_2$ in the hydration solution. Since the C-S-H growth is intertwined at different nucleation sites on the surface of the slurry mineral particles, the inter-gel pores are formed between the products of hydration.

IV: High calcium condensation and geoplymencation. As hydration progresses, the insufficiently reacted plasma of Ca^{2+}, $[AlO_4]^{5-}$, $[CaSiO_4]^{2-}$ and OH^- in the slurry and segment of the C-S-H repolymerize to form C-A-S-H. Eventually, PBM is slowly solidified and formed with new mineral crystals and C-S-H.

Preprints (www.preprints.org) | NOT PEER-REVIEWED | Posted: 30 May 2022 doi:10.20944/preprints202205.0401.v1

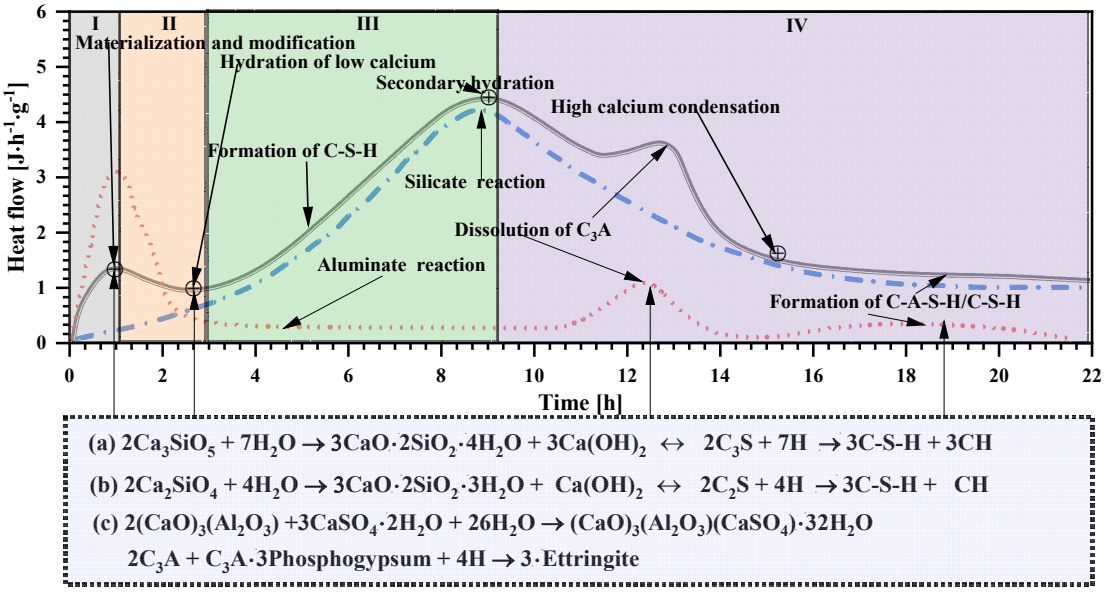

Figure 13. Rate of PBM as a function of time given by isothermal calorimetry measurement.

5. Conclusion

(1) Macro and micro experimental analysis showed that the addition of PG at the early stage promoted the formation of AFt, dissolution of C_3S, polymerization of C-S-H gels and morphological transformation. The amount of AFt crystal first increased, then decreased and then increased with the increase of PG content, and the $[SO_4]^{2-}$ generated by its dissolution could stimulate the activity of FA. The synergistic promoting effect of PG and FA was confirmed. The hydration products were generated slowly in the early stage and increased rapidly in the later stage, which AFt crystals were inserted into the C-S-H gels to make the structure of the whole hardened slurry more dense.

(2) The thermodynamic model of ECP was established, and the thermodynamic properties were simply simulated by GEMS, which can quantitatively explain the dissolution of C_3S and the formation and evolution of C-S-H gels between PG-FA mineral admixture and hydration product of PC. The values of mineral single-phase CaO, SiO_2^H and H_2O_{hyd} in hydration products gradually increase with the increasing of Ca/Si ratios. The values of CaO_{ext} and H_2O_{OH} are proportional, while the values of SiO_2^H and SiO_2 are inversely proportional.

(3) The evolution law of hydration product structure mainly is manifested that PG generates $[SiO_4]^{2-}$ ion by ionization, Ca-O-Ca and Si-O-Si covalent bonds break when alkali encounters, and combined with Si-O-Si, Al-O-Al, Al-O and Si-O covalent bonds broken by PC. At the same time, it reunited with $[SiO_4]^{2-}$ and $[AlO_4]^{5-}$ ions ionized by FA, and polymerized to form stable C-S-H and C-A-S-H hexahedral network structures.

References

[1] National Development and Reform Commission.China Resources Comprehensive Utilization Annual Report (2014) [R]. Recyclable Resources and Circular Economy, 2014.

[2] Bai L Q, Zhang Y H, Tong W S, et al. Mineral composite materials and their energy storage and energy catelysis applications [J]. Chinese Science Bulletin, 2021.

[3] HE Yaling, XIE Tao. A review of heat transfer models of nanoporous silica aerogel insulation material [J]. Chinese Science Bulletin, 2015,60(02):137-163.

[4] CHURAKOV S V, LABBEZ C. Thermodynamics and Molecular Mechanism of Al Incorporation in Calcium Silicate Hydrates [J]. The Journal of Physical Chemistry C, 2017, 121(8): 4412–4419.

[5] LOTHENBACH B, KULIK D A, MATSCHEI T, et al. Cemdata18: A Chemical Thermodynamic Database for Hydrated Portland

Cements and Alkali-Activated Materials [J]. Cement and Concrete Research, 2019, 115: 472–506.

[6] Ana Carriço, José Alexandre Bogas, Mafalda Guedes. Thermoactivated Cementitious Materials – A Review [J]. Construction and Building Materials, 2020, 250: 118873.

[7] Cédric Roosz, Philippe Vieillardc, Philippe Blancb, et al. Thermodynamic properties of C-S-H, C-A-S-H and M-S-H phases: Results from direct measurements and predictive modelling [J]. Applied Geochemistry, 2018, 92: 140-156.

[8] JOHN E, STEPHAN D. Calcium Silicate Hydrate—in-Situ Development of the Silicate Structure Followed by Infrared Spectroscopy [J]. Journal of the American Ceramic Society, 2021, 104(12): 6611–6624.

[9] KULIK D A, MIRON G D, LOTHENBACH B. A Structurally-Consistent CASH+ Sublattice Solid Solution Model for Fully Hydrated C-S-H Phases: Thermodynamic Basis, Methods, and Ca-Si-H2O Core Sub-Model [J]. Cement and Concrete Research, 2022, 151: 106585.

[10] ANDERSEN M D, JAKOBSEN H J, SKIBSTED J. Characterization of White Portland Cement Hydration and the C-S-H Structure in the Presence of Sodium Aluminate by ^{27}Al and ^{29}Si MAS NMR Spectroscopy [J]. Cement and Concrete Research, 2004, 34(5): 857–868.

[11] PANG X, MEYER C. Modeling Cement Hydration by Connecting a Nucleation and Growth Mechanism with a Diffusion Mechanism. Part II: Portland Cement Paste Hydration [J]. Science and Engineering of Composite Materials, 2016, 23(6): 605–615.

[12] KRISHNYA S, HERATH C, ELAKNESWARAN Y, et al. Modeling of Hydration Products and Strength Development for High-Volume Fly Ash Binders [J]. Construction and Building Materials, 2022, 320: 126228.

[13] ZHOU Jin, CHEN Lou, ZHENG Keren, LIU Zanqun, YUAN Qiang, HE Fuqiang. Formulating Portland cement–reactive alumina blend through thermodynamic modeling to prevent the alkali–silica reaction [J]. Journal of the American Ceramic Society, 2022, 105:1533–1547.

[14] LOTHENBACH B, ZAJAC M. Application of Thermodynamic Modelling to Hydrated Cements [J]. Cement and Concrete Research, 2019, 123: 105779.

[15] SHI Caijun, A. Fernández Jiménez b , Angel Palomo. New Cements for the 21st Century: The Pursuit of an Alternative to Portland Cement [J]. Cement and Concrete Research, 2011, 41(7): 750–763.

[16] XU Fei, WEI Hua, QIAN Wenxun, HU Shaowei, CAI Yuebo. Research on the compositional minerals of cemented soil combined thermogravimetry and thermodynamic modelling [J]. Journal of Building Materials, 2022,1-13.

[17] Cuesta A, Zea-Garcia J.D., Londono-Zuluaga D. et al. Multiscale understanding of tricalcium silicate hydration reactions [J]. Scientific Reports, 2018, 8: 8544.

[18] CUESTA A, SANTACRUZ I, DE LA TORRE A G, et al. Local Structure and Ca/Si Ratio in C-S-H Gels from Hydration of Blends of Tricalcium Silicate and Silica Fume [J]. Cement and Concrete Research, 2021, 143: 106405.

[19] YANG Nanru, YUE Wenhai. The handbook of inorganic matalloid materials atlas [M]. Wuhan: Wuhan University of Technology Press, 2000: 245-267.

[20] LIAN Huizhen. Phase research fundamental of building materials [M]. Beijing: Tsinghua University Press, 1996: 114.

[21] MUTISYA S M, DE ALMEIDA J M, MIRANDA C R. Probing the Dynamics of Water over Multiple Pore Scales in Cement by Atomistic Simulations [J]. Applied Surface Science, 2021, 565: 150426.

[22] POIRIER M, BLOTEVOGEL S, NOIRIEL C, et al. Synchrotron X-Ray Micro-Tomography Investigation of the Early Hydration of Blended Cements: A Case Study on CaCl2-Accelerated Slag-Based Blended Cements [J]. Construction and Building Materials, 2022, 321: 126412.

[23] Ghosh K, Ghosh P. Physical, mechanical, and microstructural properties of alkali-activated paste and mortar [M]. Alkali-Activated Fly Ash Blast Furnace Slag Composites. 2020: 29–134.

[24] Masoudi R, Hooton RD. Examining the hydration mechanism of supersulfated cements made with high and low-alumina slags [J]. Cement and Concrete Composites. 2019, 103:193–203.

[25] Masoudi R and Hooton R D 2019 *Cem. Concr. Compos.* **103** 193